Uncertainty Quantification in Calibration of AFM Probes Due to Non-uniform Cantilevers

Hendrik Frentrup

under the guidance of

Prof. Matthew S. Allen, Ph.D.
Department of Engineering Physics - College of Engineering
University of Wisconsin-Madison

April 2010

Abstract

For more than two decades, the Atomic Force Microscope (AFM) has provided valuable insights in nanoscale phenomena, and it is now widely employed by scientists from various disciplines. AFMs use a cantilever beam with a sharp tip to scan the surface of a sample both to image it and to perform mechanical testing. Since the AFM measures the deflection of the probe beam, one must first find the spring constant of the cantilever in order to estimate the force between the sample and the probe tip. Commonly applied calibration methods regard the probe as a uniform cantilever, neglecting the tip mass and any non-uniformity in the thickness along the length of the beam. This work explores these issues, recognizing that dynamic calibration boils down to finding the modal parameters of a dynamic model for a cantilever from experimental measurements and then using those parameters to estimate the static stiffness of a probe; if the modes of the cantilever do not match the expectations, for example because non-uniformity was neglected, then the calibration will be in error. This work explores the influence of variation in the thickness of a cantilever probe on its static stiffness as well as its dynamics, seeking to determine when the uniform beam model that is traditionally employed is not valid and how one can make sure whether the model is valid from measurable quantities. In this study, the implications for two commonly applied dynamic calibration methods, the method of Sader and the Thermal Tune method, were explored. The results show that the Sader method is quite robust to non-uniformity so long as only the first dynamic mode is used in the calibration. The Thermal Tune method gives significant errors for the non-uniform probe studied here.

Contents

Nomenclature

Latin letter

A	Cross-section area of the cantilever
b	Cantilever width
$\mathbf{C}$	Damping matrix
d_c	Amplitude of vibration at the end of the cantilever
E	Young's modulus
F	Force
h	Cantilever thickness
I	Second moment of area
$\mathbf{K}$	Stiffness matrix
k_s	Spring constant
k_B	Boltzmann's constant
L	Cantilever length
$\mathbf{M}$	Inertia matrix
m	Mass
M	Moment
M_e	Effective normalized mass
$\mathbf{q}$	Generalized coordinates
$\mathbf{Q}$	Generalized forces
q_z	Force per unit length
Q	Quality factor
s	Distance on a defined path
S	Shear force
T	Temperature
w	Deflection
W	Static deflection
x	Coordinate along beam axis

Greek letter

α_n	n^{th} frequency parameter
Γ	Hydrodynamic function
ρ	Cantilever density
ρ_{f}	Density of the surrounding fluid
$\mathbf{\Phi}_n$	n^{th} normalized mode shapes
χ	Optical lever factor
ψ_n	n^{th} basis function
ω_n	n^{th} natural frequency

Subscript

beam	Property of the beam
es	Equivalent value in the context of the static stiffness
ek	Equivalent value within the stiffness coefficients
em	Equivalent value wihtin the inertia coefficients
end	Property of an end-loaded cantilever
f, fluid	Property of the fluid
free	Property of a freely vibrating cantilever
i	Imaginary part
measured	Measured quantity
nom	Nominal value
r	Real part
tip	Property of the tip
vib	Property of vibration
obs	Observed value

Superscript

exp	Experimental value
model	Property of the model
true	Actual property

Abbreviations

AFM	Atomic Force Microscope
ODE	Ordinary Differential Equations
PDE	Partial Differential Equation

PSD	Power Spectral Density
SEM	Scanning Electron Microscope
SHO	Simple Harmonic Oscillator
STM	Scanning Tunneling Microscope

1. Introduction

Originally designed to measure conductors and insulators on an atomic scale, the inventors of the Atomic Force Microscope (AFM) envisioned a device that could be applied to measure forces and examine surfaces in many fields of science [3]. A great advantage of the AFM is the fact that the sample of interest need not be coated, measured in vacuum or conduct an electrical current. AFMs can also operate under ambient conditions. Hence, the range of applications for an AFM are enormous and allow for quantitative research on the nanoscale where other microscopic methods are far beyond their limits. Today, the AFM is indeed useful to scientists in the fields of medicine, biotechnology, chemistry, engineering and many more.

A particularly spectacular example for the potential of the AFM is the imaging of single atoms within a pentacene molecule [15], shown in figure 1. It is necessary to perform the imaging near the absolute zero and under ultra-high vacuum conditions. Moreover, the tip of the AFM needs to be sharpened by picking up a CO molecule to achieve this level of resolution. Nonetheless, these dimensions were only explored in a theoretical realm before. Recently, the AFM also rendered possible the manipulation of single atoms on a semiconductor surface at room temperature [23]. Sugimoto et al. [23] describe how they implemented co-called dip-pen nanolithography with the AFM. The tip apex is wetted with atoms which could then be individually deposited to write patterns on the semiconductor surface. These examples show how important of a role the AFM plays in the development of nanoscale electronics and chemistry. What is more, AFM techniques

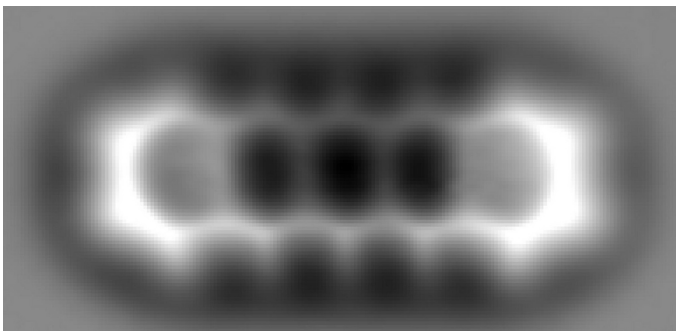

Figure 1.: AFM image of pentacene molecules with unprecedented atomic resolution by probing the short-range chemical forces with use of non-contact atomic force microscopy, performed at IBM Research Zurich.

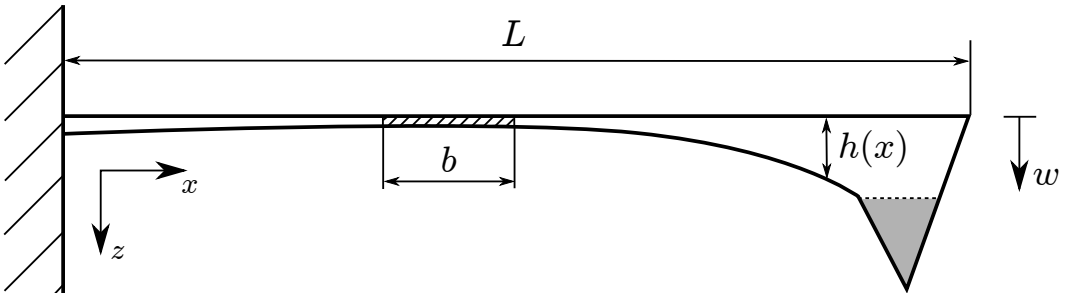

Figure 2.: Schematic shape of a cantilever with sharp tip. L denotes the cantilevers length, b its width. The thickness h of the cantilever is not uniform over the cantilevers length, but a function $h(x)$ along its length. The cantilever above is not drawn to scale and the thickness variation is overemphasized. The deflection of the cantilever along the x-axis is given by $w(x,t)$.

are commonly employed in microbiology for their advantage over electron microscopy when measuring living organisms. Only under conditions where the organisms prosper is it possible to directly observe their cell growth [25]. Hence, measurements on living cells have to be done in aqueous solutions in order to observe dynamic events on this scale, such as the interaction between cell membranes and drugs [10]. Structural imaging being one useful application, force spectroscopy is also increasingly being used in microbiology to measure the nanoscale chemical and physical properties of cells. The practical potential of force spectroscopy is demonstrated in a study on the nanomechanical properties of cancer cells [9]. AFM indentation on metastatic cancer cells discovered a significantly lower stiffness compared to benign cells despite their morphological similarity, suggesting that the AFM might be more effective for cancer screening than visual inspection of the cells.

To achieve this widespread use, AFMs employ a cantilever beam with a sharp tip at its end that is used to scan the surface of the sample or sense the object of interest in force spectroscopy. A crucial part of performing AFM measurements is therefore the calibration of the microscopes. To find the force exerted on the tip of the cantilever beam, the deflection of the beam is measured and the respective force can be calculated when the stiffness of the beam is known.

Today, a range of different calibration techniques exist. Among these, dynamic methods, which determine the static stiffness from the cantilevers vibration response, have practical advantages. Two dynamic methods are commonly applied to determine the stiffness of the beam. Sader's method [18] measures the damping of the beam vibrating in air and uses a model for the fluid-structure interaction to compute the calibration constant. The Thermal Tune method [16] determines the stiffness from measurements of the natural frequency and amplitude of vibration of the beam when it is subject only to thermal excitation.

For simplification, these methods usually regard the beam to be a cantilever beam of uniform thickness and equal mass distribution. They neglect, as it is exemplified in figure 2, the tip mass of the actual beam and that the beam has a varying thickness along its length. The objective of this study is a contributution to the development of a more accurate and reliable model underlying these calibration methods [11].

In particular, the study focuses on the non-uniform shape of the beam and its influence on the calibration process. Non-uniformity was examined for static and dynamic behavior. A Ritz model was created to capture the dynamic behavior of non-uniform beams. Based on this model, the calibration methods were modified and the previous methods were compared to these modified schemes. As a result of this comparison, the deviations between modified and original schemes are presented and the calibration errors quantified.

1.1. Mode of operation of the AFM

The development of Scanning Probe Microscopy was initiated by the Scanning Tunneling Microscope (STM) [4] in 1982 at IBM Research in Zurich. The STM uses the tunneling current between a probe tip and the sample surface to determine the distance between tip and surface. Thus, both tip and sample must be conductive [17]. The inventors received the Nobel Prize for this invention in 1986. In the same year, the first Atomic Force Microscope was built by the Nobel laureates.

Compared to its precursor, the AFM works in a much more intuitive way. The AFM uses a sharp tip mounted on a small cantilever beam to scan over the surface of a sample. While scanning the sample, the deflection of the microcantilever is measured by pointing a laser at its free end and recording the motion of the reflected laser spot with a photodiode [10]. Figure 3 provides an image of this mechanism.

With help from a calibration sample, it is possible to determine the relationship between the voltage output of the diode and the cantilever's deflection, called deflection sensitivity. Various modes of operation have been developed until today. Initially, the AFM worked in contact mode, where the probe's tip is in contact with the sample [22]. Dynamic modes of operation prevent the tip from being damaged and worn out. Dynamic operation implies that the dynamic behavior of the cantilever is exploited to determine the distance between tip and sample without being in contact. The Van der Waals forces inflicted on the cantilever have an influence on its natural frequency and its amplitude of oscillation. The changes in vibration behavior are recorded during the measurements and then exploited to acquire the topology of the sample of interest or to calculate the acting forces.

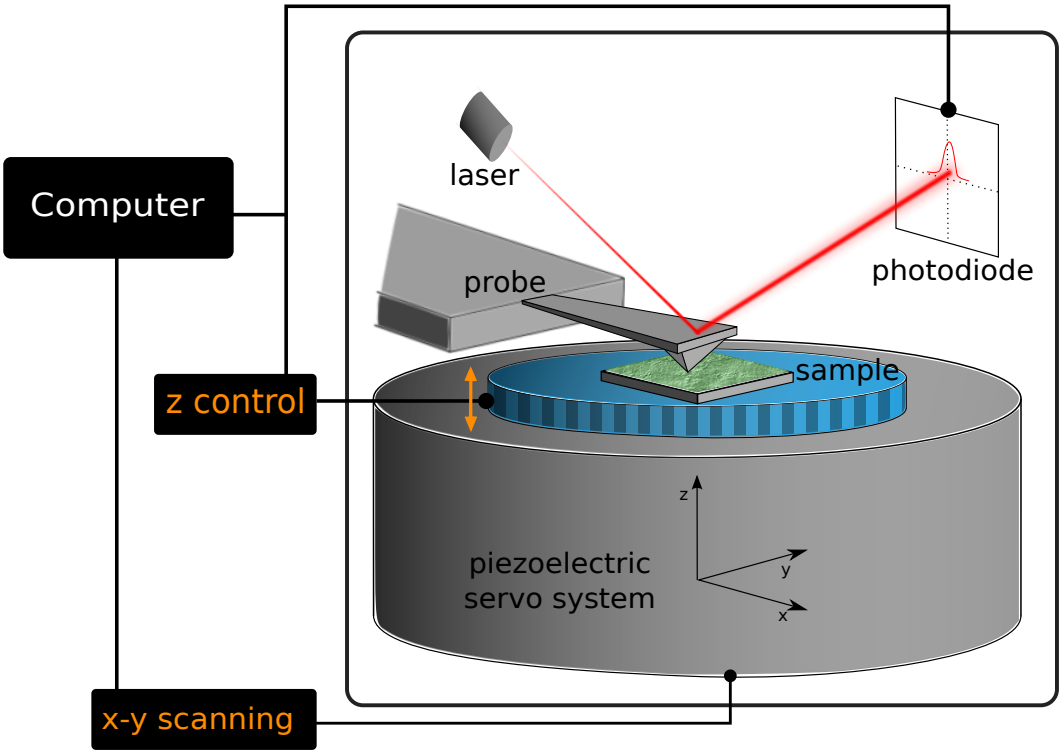

Figure 3.: Schematic description of the AFM mechanism. The laser beam is the reflected from the cantilever to the photodiode. The stack of computer-controlled piezoelements moves the sample under the cantilever probe and allows the scanning of the surface.

2. Dynamic Calibration Methods

With the deflection sensitivity determined from imaging a calibration sample, the voltage output of the photodiode is related to the deflection of the cantilever. A second calibration must be performed if one wishes to relate the measured deflection to the tip-sample force, depicted in figure 4. Since a mechanical model is necessary for this step, the present study focuses precisely on the second type of calibration.

The spring constant, i.e. the static stiffness of the cantilever, is the parameter that must be determined to find the forces of interest. The deflections of the vibrating cantilever are small and one can assume that they are linear. Therefore, classical beam theory is a valid approach. Accordingly, the spring constant of a uniform cantilever, $k_s = {}^{Ebh^3}/_{4L^3}$, depends on its Young's modulus E and it's geometry, with b being the cantilever's width, L its length [21]. In detail, $k_s = {}^{3EI}/_{L^3}$, where I is the beam's second moment of area $I = {}^{bh^3}/_{12}$. The thickness of the beam, h, is typically assumed to be uniform along the length. Due to considerable variations in microfabrication, the properties of the cantilevers, especially Young's modulus, thickness and mass distribution, cannot be determined very easily. Calibration is therefore of crucial importance in force spectroscopy, and even in routine contact-mode or friction force imaging, if one needs to know the force applied by the probe during imaging.

In the process of determining the static stiffness of an AFM probe, one faces the challenge that the cantilevers and especially their tips are very delicate structures. A sharp tip is usually very important for AFM measurements and the static loading can inflict damage

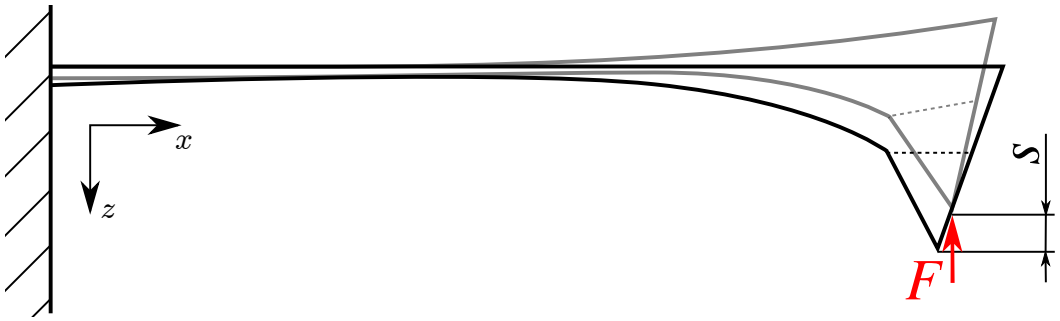

Figure 4.: The static stiffness is the relationship between the path distance of the cantilever's deflection s and the force F exerted on the cantilever's tip that is causing the deflection.

to the probe. To be practical, AFM calibration methods must not damage the probes in the calibration process and one must be able to perform them quickly and without the need for additional complex equipment other than the AFM. Moreover, effective calibration methods must be applicable under ambient conditions, as the AFM usually operates at such. Thus, a wide range of non-invasive methods have been developed [5], such as the method by Cleveland et al. [7] where the spring constant can be determined by measuring the cantilevers resonant frequencies before and after adding small masses at its end. This method entails the meticulous task to add and remove microscopic masses to the cantilever. To circumvent this issue, dynamic methods that are quicker and easier to perform have prevailed. The focus of this work is on two non-destructive, dynamic calibration methods, the Sader method and the Thermal Tune method. Both methods need no extra equipment, as the AFM itself can measure all quantities needed for calibration.

2.1. Sader Method

The frequency response of a cantilever beam was commonly simplified to the response of a simple harmonic oscillator (SHO) and many dynamic calibration techniques are based on this idea. When regarded as such, the spring constant of the cantilever depends on its mass, i.e. its density and dimensions, and radial natural frequency.

$$k_{\mathrm{s}} = m_{\mathrm{e}}\,\omega_1^2 = M_{\mathrm{e}}\,\rho\,hbL\,\omega_1^2 \tag{1}$$

k_{s} denotes the beam's static stiffness, ω_1 its first radial resonant frequency, and ρ denotes its density. The effective mass m_{e} of the cantilever is used to bring the model in alignment with the simplification of being a SHO. An extensive discussion of M_{e}, the beam's normalized effective mass, is given by Sader et al. [20][1].

The dimensions of an AFM probe range between 100 to 500 μm in length, from 15 to 50 μm in width and often less than a micrometer in thickness. Therefore, the cantilevers planview dimensions, i.e. the width and length, can be determined using optical microscopy, and thus it does not pose a limitation for the calibration. Nonetheless, accurately determining the thickness of the cantilever typically requires the use of an electron microscope. Scanning Electron Microscopy (SEM) is a very expensive technique and the process might inflict damage to the probe and severly impair further usage. Moreover, the density of silicon nitride cantilevers is highly variable and assuming it as a given parameter would introduce a large error into the calibration process.

[1] M_{e} is approximately equal to 0.2427 for $L/b > 5$.

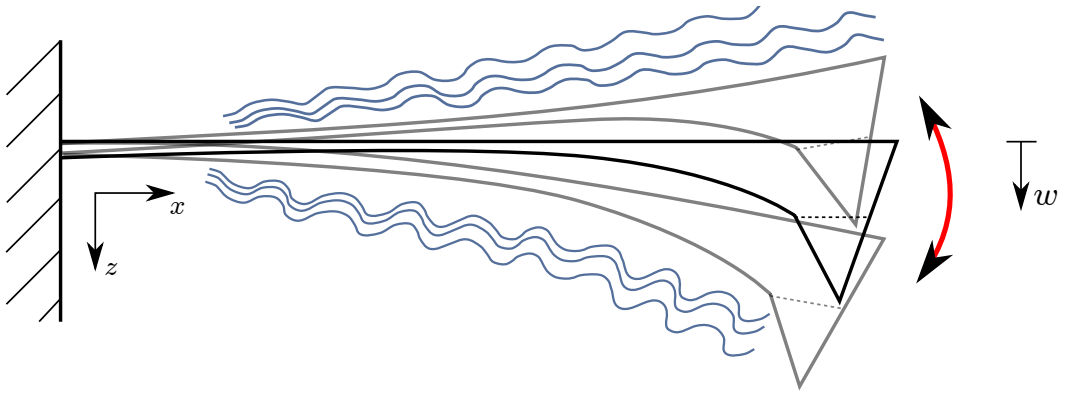

Figure 5.: The vibrating cantilever moves the fluid surrounding it, depicted by the blue wavy lines.

On another note, equation (1) only holds true if the cantilever is vibrating in vacuum. As shown in figure 5, an oscillating cantilever immersed into a fluid moves the surrounding fluid as it vibrates, creating an inertial loading on the beam, a virtual mass. The resonance frequencies of an immersed cantilever are lower compared to a cantilever in vacuum due to the inertial loading. The surrounding fluid also has an external damping effect on the cantilever. This lowers the cantilever's quality factor Q by reducing the peak amplitude and broadening its resonance curve[1]. It also affects the phase response by reducing its steepness [12].

Sader developed his method by taking the effects of the surrounding fluid, in most cases air, on the oscillating cantilever into account [20]. He uses the natural frequency and Q factor of the first mode of the cantilever to determine its static stiffness. Sader accounted for these effects by including a hydrodynamic force as part of the loading on the vibrating cantilever [18]. According to Sader, the complex amplitude $F(x,\omega)$ of the harmonic load $\hat{F}(x,t) = F(x,\omega)\mathrm{e}^{\mathrm{i}\omega t}$ consists of the driving load and a hydrodynamic force.

$$F(x,\omega) = F_{\mathrm{hydro}}(x,\omega) + F_{\mathrm{drive}}(x,\omega) \tag{2}$$

$$F_{\mathrm{hydro}}(x,\omega) = \frac{\pi}{4}\rho_{\mathrm{f}}\omega^2 b^2 \Gamma(\omega) w(x,\omega) \tag{3}$$

The hydrodynamic force is a function of vibration frequency of the cantilever ω, the density of the surrounding fluid ρ_{f}, the beam's width and the normalized hydrodynamic load, called hydrodynamic function $\Gamma(\omega)$, which can be obtained from solving the equations of motion for the surrounding fluid [18, 19]. As mentioned above, it can be seperated into an inertial term, the real part of the hydrodynamic function $\Gamma_{\mathrm{r}}(\omega)$,

[1]The quality factor Q is a measure for the damping ratio ζ of the system, $\zeta = \frac{1}{2Q}$.

and a dissipative term given by its imaginary part $\Gamma_{\mathrm{i}}(\omega)$. The derivation according to Sader [19] yields

$$k_{\mathrm{s,Sader}} = 0.1906 \rho_{\mathrm{f}}\, b^2 L\, \Gamma_{\mathrm{i}}\, Q\, \omega_1^2. \tag{4}$$

Some information on the cantilever's geometry is still required to use the Sader method, namely the planview dimensions of a rectangular cantilever which govern the effects of the fluid for flexural oscillations. However, Sader assumed a uniformly thick cantilever in his derivation and did not take any tip mass into account. Allen et al. [2] pointed out that these assumptions are not accurate and, depending on the mode used for the calibration, can lead to errors of considerable extent in the calibration process. They quantified the error in the stiffness estimated by the Sader method due to an unmodeled rigid tip and proposed a method that can be used to estimate the tip mass from measurements of the natural frequencies of the probe. The tip was found to cause considerable calibration error for some AFM probes if not correctly accounted for. This work explores the effect of a non-uniform thickness along the cantilever's length on its dynamic properties and the implications for the accuracy of dynamic calibration methods. The tip at the cantilever's end is also taken into account.

2.2. Thermal Tune Method

The Thermal Tune method, first proposed by Hutter and Bechhoefer [16], exploits the equipartition theorem to determine the spring constant. The theorem states that the kinetic or potential energy of each mode of a cantilever when excited by only thermal noise, induced by Brownian motion (as seen in figure 6), is equal to $1/2\, k_{\mathrm{B}}T$ [5], with T being the absolute temperature and k_{B} being Boltzmann's constant. This relationship is used to relate the mean-square thermal noise oscillation amplitude with the spring constant,

$$\langle E \rangle = \frac{1}{2} k_{\mathrm{s}} \langle d_{\mathrm{c}}^2 \rangle = \frac{1}{2} k_{\mathrm{B}} T, \tag{5}$$

with $\langle d_{\mathrm{c}}^2 \rangle$ being the mean-square amplitude of the cantilever's thermal fluctuation.

Although the method appears quite simple, there are a number of important details that must be accounted for, as described by Cook et al. [8]. Unlike the assessment of the deflection sensitivity, which is measured under static conditions, the Thermal Tune calibration is performed on a vibrating cantilever. There is a discrepancy between the way a statically deflected and a vibrating cantilever reflect the laser. With respect to this issue, the method was enhanced by Butt and Jaschke [6]. Additionally, the laser spot is

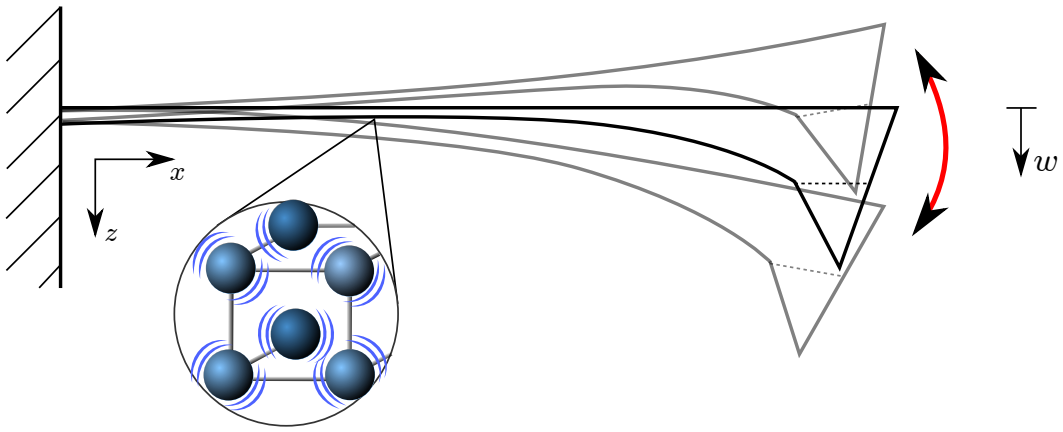

Figure 6.: The source of thermal noise vibrations is the Brownian motion of the silicon nitride lattice the cantilever consists of.

not infinitely small, it rather extends over a section of the beam along it's length. Again, the model the existing method is based on makes the assumption that the cantilever has a constant thickness and no tip at its end.

2.3. Measuring the vibration response of a microcantilever

Generally, the first step of calibration is the capturing of a power spectrum of a freely vibrating cantilever with no excitation acting on it. While the Sader method can also be performed for a driven cantilever, the Thermal Tune method relies on only thermal excitation. The measurement of the power spectrum can be performed with the AFM itself. In many cases, it is useful to employ an oscilloscope with a high sampling rate. The captured signal is Fourier transformed to the detector-voltage power spectral density (PSD). The required natural frequency and the quality factor can be obtained from this voltage PSD by fitting a SHO response, R, with an added background term B to the signal, depicted in figure 7:

$$B + R(\omega) = B + \frac{A_n \omega_n^4}{(\omega^2 - \omega_n^2)^2 + (\frac{\omega\omega_n}{Q_n})^2} \tag{6}$$

The Thermal Tune calibration requires an extra step. The amplitude of the thermal vibration response is measured in voltage. With an accurately determined deflection sensitivity, the cantilever's response can be converted to actual deflection. A force curve is acquired with the cantilever to perform this conversion, and the mean-square deflection is calculated from the converted response signal.

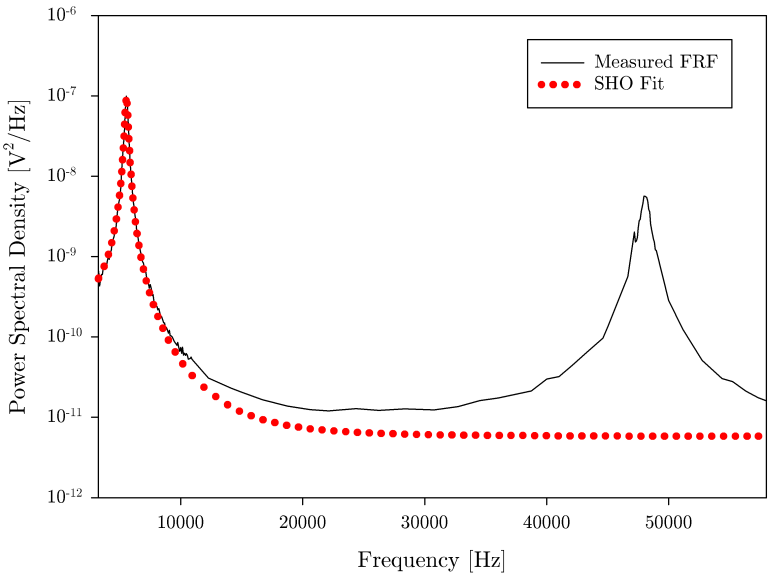

Figure 7.: Power spectral density of the thermal vibration response of a microcantilever with the respective fit to cantilever's first mode.

3. Influences of Non-Uniformity

Many commercially available AFM probes are significantly non-uniform along their lengths. For example, the SEM images shown in figure 8 were obtained from a CSC38-B cantilever manufactured by Mikromasch. The nominal thickness of the beam is given by the manufacturer as 1 μm. The SEM images indicate that the thickness of the cantilever is not uniform but has a considerable taper toward the tip. It is almost three times as thick as nominal at the point where the tip starts. The profile of the beam was estimated using these SEM images and will be used to quantify the effect of this thickness non-uniformity on calibration for this particular probe, with a view to extending the methodology to other probes.

The mechanics of the measured cantilever profile will also be compared to two different profiles that approximate it with a small number of parameters. The first models the non-uniformity with a section that has constant thickness, h_{nom} with a taper starting at x_0, and reaches the same thickness as the real cantilever at the free end. This profile will be called the "partially linear" profile. The second models the non-uniformity as a linearly increasing thickness. This profile cannot mimic the prominent increase in thickness that the real profile has at the end of the cantilever, so that part is regarded as an extra mass without rotary inertia and lumped at the end of the cantilever. This latter profile shall be referred to as "linear and lumped". The chosen profiles and the actual profile from the SEM images are depicted in figure 9. Both parametrizations are defined by only three parameters, which are given in table 1. The "linear and lumped #2" profile is a result of the sensitivity analysis described in section 3.2.2. Its parameters were chosen to match the experimental result of the frequency spacing more closely, whereas the parameters for the "linear and lumped" profile were chosen based on the SEM images shown previously. More complicated profile models could be envisioned, but then one would have more free parameters that must be either assumed or determined.

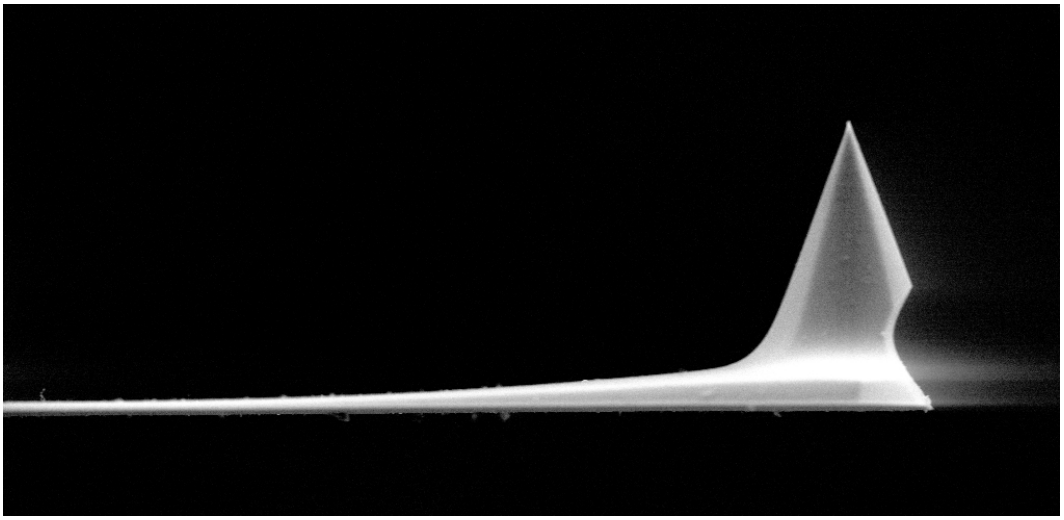

(a)

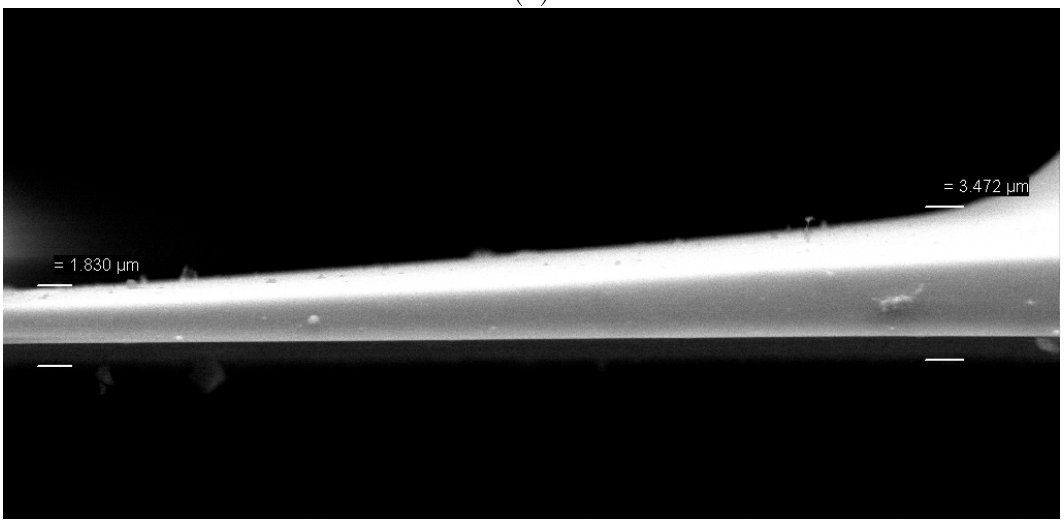

(b)

Figure 8.: SEM images of a silicon nitride cantilever beam. In (a), the tip and a portion of the cantilever are shown. In (b), a detail near the tip is shown where it can be observed how the thickness of the cantilever increases from 1.830 μm to 3.472 μm toward the tip.

Profile parameters			
Partially linear	$h_{\text{nom}} = 1.0\,\mu\text{m}$	$h(1) = 3.876\,\mu\text{m}$	$x_0 = 0.83$
Linear and lumped	$h_0 = 1.218\,\mu\text{m}$	$h_1 = 0.275\,\mu\text{m}$	$\Delta m = 5.792 \cdot 10^{-12}\,\text{kg}$
Linear and lumped #2	$h_0 = 1.193\,\mu\text{m}$	$h_1 = 0.302\,\mu\text{m}$	$\Delta m = 6.372 \cdot 10^{-12}\,\text{kg}$

Table 1.: The parameters of the two chosen profiles fitted to the real cantilever profile. The definition of the parameters is given in section A.1 of the appendix.

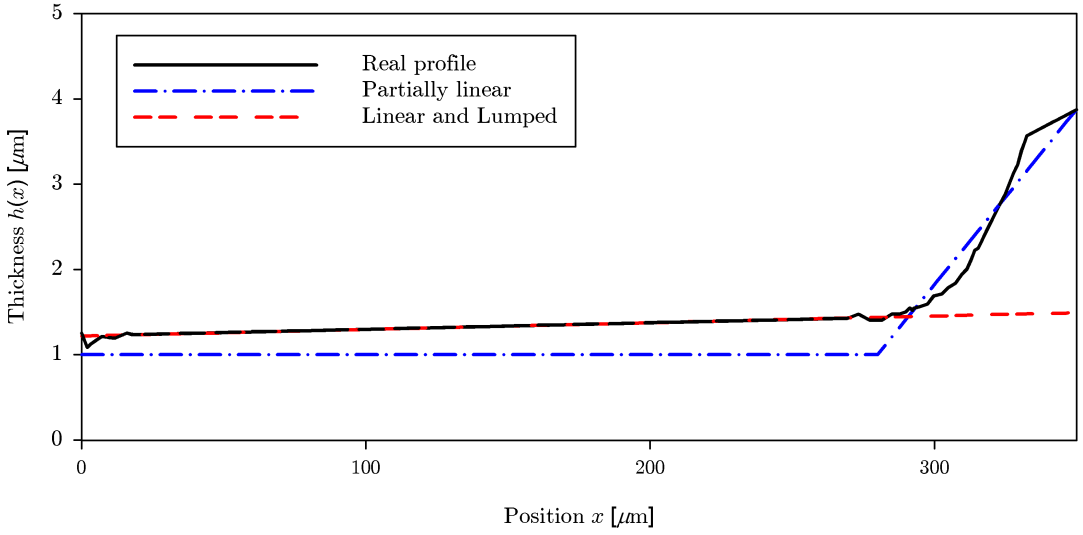

Figure 9.: Different thickness profiles of the cantilever beam. The estimate of the actual profile and two fitted counterparts are shown.

3.1. Static Properties

In order to determine how well each of these models captures the static stiffness of the cantilever, an analytical solution was derived for the spring constant of a cantilever with an arbitrary thickness variation along its length. The deflection curve of the cantilever is given by $w'' = {}^{M(x)}/_{EI(x)}$, with M being the bending moment acting on the cantilever. Loaded with a static tip force, the bending moment is linear. Thus, one can express the spring constant as follows (for a thorough derivation, see section A.2 in the appendix)

$$k_\mathrm{s} = \frac{Eb h_\mathrm{es}^3}{4L^3}, \tag{7}$$

$$h_\mathrm{es}^3 = -\frac{1}{3}\left[\int_0^1 \int_0^{\tilde{x}} \frac{(\tilde{x}-1)}{h(\tilde{x})^3}\mathrm{d}\tilde{x}\mathrm{d}x\right]^{-1}. \tag{8}$$

This expression is comparable to the expression for a uniform cantilever only that the equivalent thickness h_es, used to describe a non-uniform cantilever, is the thickness a uniform cantilever of the same static stiffness would have.

The static stiffnesses computed for each of the probe models using this approach are shown in Table 3. The manufacturer estimated the spring constant of the cantilever at $0.03\,{}^\mathrm{N}/_\mathrm{m}$, presumably based on the nominal thickness of $1\,\mu$m, and the analytical model agrees well with this. However, the manufacturer also states that the spring constant could be anywhere in the range from only a third to more than twice the nominal value.

Cantilever Model	k_s [N/m]
Uniform + Tip	0.0278
Measured profile	0.0580
Partially linear	0.0278
Linear and lumped	0.0585
Linear and lumped #2	0.0560
Manufacturer's specification: $k_s = 0.03\ (0.01 - 0.08)$ N/m	

Table 2.: Static stiffness, k_s, estimated for each of the models of the thickness profile.

In fact, the profile from the SEM images has a spring constant of 0.058 N/m which is almost twice the nominal value. The static behavior of the other parameterizations of the model is entirely different from each other. The considerable taper toward the free end of the beam has no noticeable effect on the beam's static stiffness as the "partially linear" spring constant is equal to that of the uniform cantilever. On the other hand, the static stiffness of the "linear and lumped" profile agrees very well with that of the measured profile.

3.2. Dynamic Properties

3.2.1. Analytical Mode Shapes of a Uniform Cantilever Beam

Dynamic calibration methods are derived from the equations of motion of an oscillating cantilever and depend greatly on its modal properties, namely the mode shapes of the cantilever. Thus, the effect of non-uniformity on the dynamics of the calibration model are of utmost importance. A derivation of an analytical solution of a uniform beam with a tip helps in the further examination of these effect. Thus, the uniform case was considered first.

The flexural motion of a beam is one of the most traditional problems in Mechanics of Materials [24]. The Euler-Bernoulli beam theory is a basic approach to the problem, by combining strain-displacement relationships and a constitutive law with the equations for dynamic equilibrium to yield the displacement field of the beam. As the length of the beam is much longer than it's cross-sectional dimensions, the classical Euler-Bernoulli beam theory can be used. Hence, the equation governing the displacement field[1] is

$$\frac{\partial^2}{\partial x^2}\left(\frac{EI}{L^4}\frac{\partial^2 w}{\partial x^2}\right) + \rho A\ddot{w} = q_z\ , \tag{9}$$

[1]Dotted quantities represent a derivative with respect to time t: $\ddot{w} = \partial^2 w/\partial t^2$

where A the cross-section area of the cantilever, and q_z denotes the force per unit length loading [14]. For now, these properties are considered to be constant along the beam's length. One can also assume that no external loads act on the beam since the eigenmodes of the strucuture are of interest at this point. It is also worth noting that the non-dimensional coordinate x is used for simplification. With a seperation of variables approach, the problem can be simplified[1] to an ordinary differential equation,

$$\psi'''' - \alpha_n^4 \psi = 0 \ , \quad \text{with} \quad \alpha_n = \sqrt[4]{\frac{\rho A \omega_n^2 L^4}{EI}} \ , \tag{10}$$

where α_n denotes the n^{th} frequency parameter. Equation (11) is the well-known solution to this problem.

$$\psi_n(x) = \sin(\alpha_n x) + \sinh(\alpha_n x) + R_n \left[\cos(\alpha_n x) + \cosh(\alpha_n x)\right] \tag{11}$$

$$R_n = -\frac{\sin(\alpha_n) + \sinh(\alpha_n)}{\cos(\alpha_n) + \cosh(\alpha_n)}$$

The correct application of boundary conditions is crucial for the problem as they determine the modal parameter α_n [2]. At the left boundary, the fixed end has no deflection or rotation. The boundary conditions on the right end are more complex. With a tip attached to the beam, shear forces and moments act on the cantilever. A balance of these loads yields the adequate set of boundary conditions. A detailed discussion is given in the appendix (see section A.3). The mass and inertia of the tip, which is being treated as a cone of height H and base radius R, are paremeters in the boundary conditions and they are given by [13]

$$m_{tip} = \frac{\pi}{3} \rho R_{\text{tip}}^2 H_{\text{tip}} \ , \qquad J_{tip} = \frac{3}{80} m_{tip} \left(4R_{tip}^2 + L_{tip}^2\right) \ . \tag{12}$$

Applying the boundary conditions correctly, one obtains the modal parameters that govern the mode shapes. The mode shapes of the cantilever with a tip whose mass is 10.3 per cent of the beam's mass are given in figure 10 [2, 11]. Recalling the definition of the modal paramteres in eq. (10), the natural frequencies of the cantilever can also be determined at this point. The values for ω_n and α_n are given in table 3 and the first four mode shapes can be seen in figure 10.

[1] Primed quantities represent a spatial derivative with respect to x: $\psi'''' = \partial^4\psi / \partial x^4$

Modal parameter α_n				
n	1	2	3	4
α_n	1.7380	4.4239	7.4828	10.5629
$\omega_n/2\pi$	9.088 kHz	58.846 kHz	168.192 kHz	334.677 kHz

Table 3.: Modal parameters

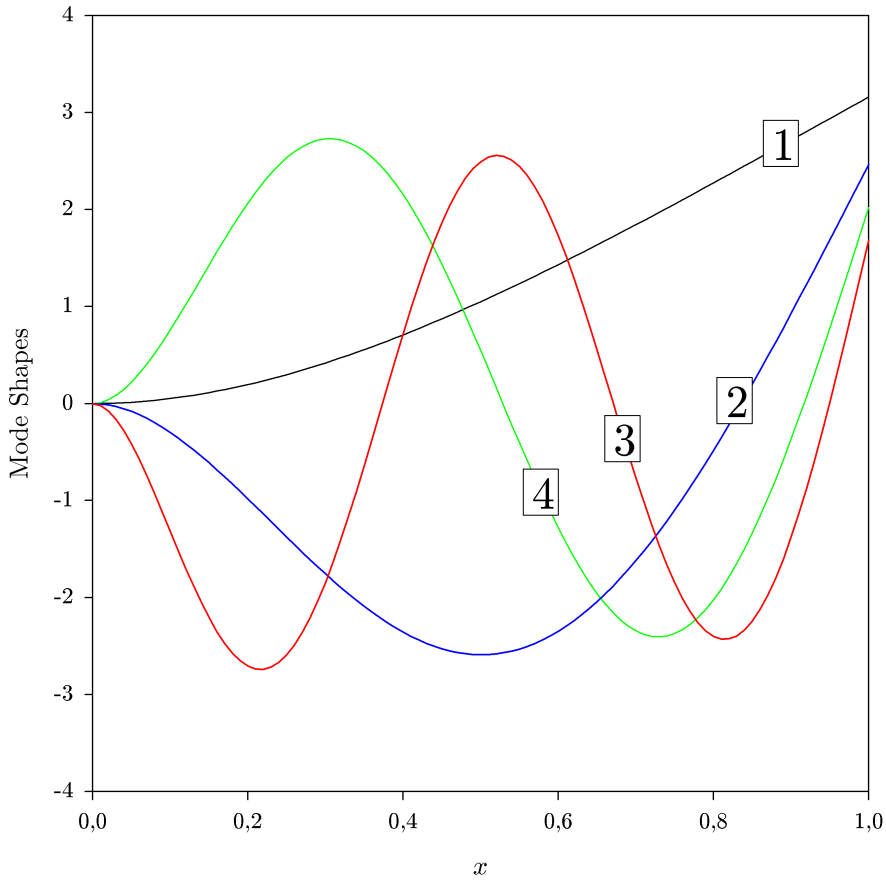

Figure 10.: Analytical mass-normalized mode shapes of a uniform cantilever with tip.

3.2.2. Ritz Method

Since the beam is a continuous structure, a Ritz model, which discretize the continuous beam into a dynamic system with a finite number of degrees of freedom, was created for each of these profiles in order to calculate mode shapes and natural frequencies for the different profiles. The equations of motion governing the motion of the cantilever are given in (13), where $\mathbf{q}$ denotes the frequency domain amplitude of the generalized coordinates [14]. The inertia and stiffness of the beam as well as the virtual mass added by the fluid and the dissipative effect of the fluid are included in the calculations (see section A.4 in the appendix for details).

$$-\omega^2[\mathbf{M}]\mathbf{q} + \mathrm{i}\omega[\mathbf{C}]\mathbf{q} + [\mathbf{K}]\mathbf{q} = 0 \tag{13}$$

The Ritz method can be used to obtain approximate solutions for the mode shapes and natural frequencies of continuous structures. Here this approach is used to find the approximate mode shapes of non-uniform cantilevers. However, later we shall make use of the fact that a single term Ritz model is an exact model for the contribution of a single mode to a structure's response if the mode shape used in the Ritz series is exact.

The analytical model gives the mode shapes of a uniform cantilever [14] with a rigid tip on its free end. Those analytical mode shapes will be used in this work as basis functions for the Ritz method in order to find the modes of the cantilever for each of the thickness profile models in Table 1. The parameters α_n depend on the boundary conditions which include the effect of the tip. In order to account for non-uniformity, the model used here allows for a variable thickness along the cantilever's length, $h = h(x)$.

Figure 11 shows the mode shapes of a cantilever with a tip mass of $m_{\mathrm{tip}} = 2.638\,\mathrm{ng}$ and a uniform nominal thickness compared to those with the same tip and the thickness profile estimated from the SEM images. The third set of mode shapes shown are for the "linear and lumped #2" model described in table 1. The mode shapes in Figure 11 indicate lower amplitudes of vibration at the end of the beam for the “linear and lumped #2” cantilever profile than for the other two because the additionally lumped mass increases the inertia of the beam at the free end. Also, the higher the order of the mode, the more the respective mode shapes are curved, in particular close to the free end of the beam, so thickness non-uniformity has a more prominent effect on the higher modes.

The spacings between the natural frequencies for all of these models are shown in Table 4. By comparing the frequency spacings rather than the frequencies, the comparison is not dependent on the modulus, density, and other physical properties of the probe. The analytical model of the uniform cantilever with tip underestimates the spacings

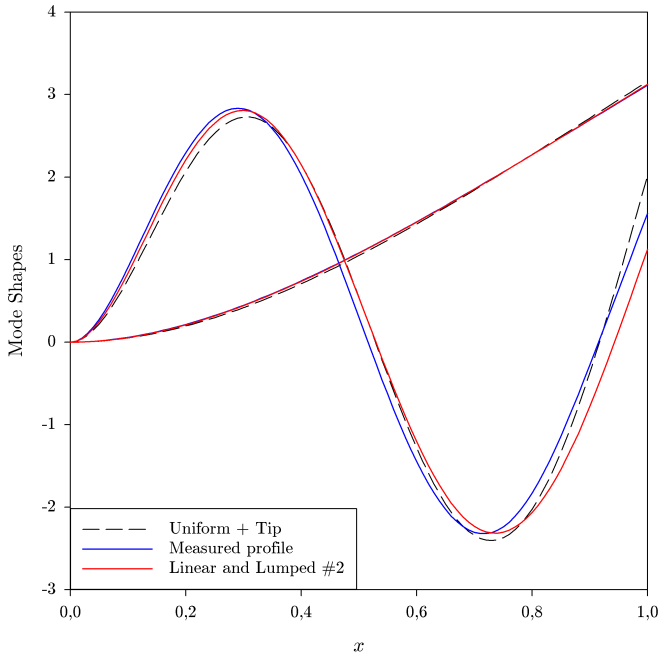

(a)

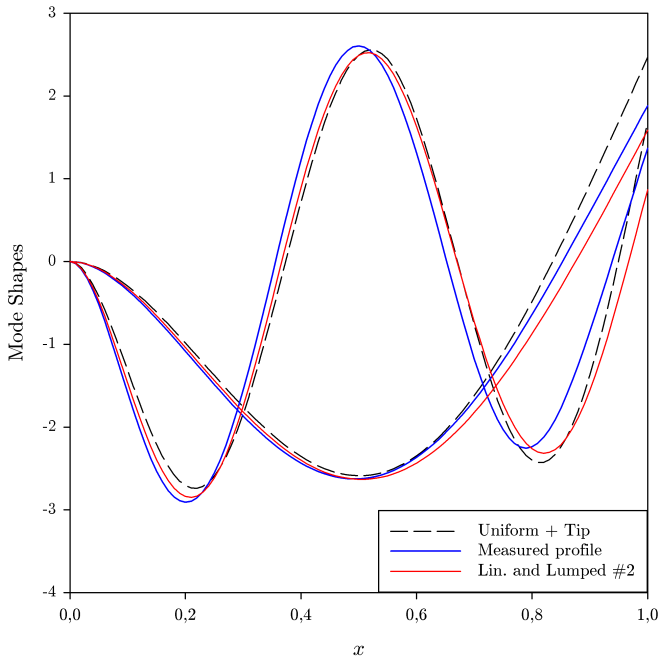

(b)

Figure 11.: Mode shapes of the cantilever. The dashed lines depict the analytical mode shapes of a uniform cantilever with tip - solid lines are Ritz estimates of the mode shapes for the measured profile and for the "linear and lumped #2" profile. The odd modes are shown in (a), even modes in (b).

	ω_2/ω_1	δ^{exp}	ω_3/ω_1	δ^{exp}	ω_4/ω_1	δ^{exp}
Experimental [2]	7.806	-	23.572	-	48.490	-
Uniform + Tip	6.475	-17.05%	18.507	-21.49%	36.826	-24.05%
Measured profile	7.807	0.01%	23.665	0.39%	48.409	-0.17%
Partially linear	7.813	0.09%	23.698	0.53%	48.964	0.98%
Linear and lumped	7.658	-1.89%	23.056	-2.19%	46.771	-3.54%
Linear and lumped #2	7.812	0.08%	23.642	0.30%	48.042	-0.92%

Table 4.: Frequency spacings of the cantilever beam. δ^{exp} is the deviation of the respective frequency spacing compared to the experimental value.

between the modes considerably and with increasing deviation for higher modes. The model that uses the measured profile reproduces the frequency spacings with a very high accuracy. The partially linear profile is almost as accurate as the measured profile while the "linear and lumped" profile presents higher deviations, but both are significantly more accurate than the uniform model with a tip. The parameters for the "linear and lumped #2" model were chosen to minimize the difference in the frequency spacings, so the agreement is excellent. One can achieve good agreement in terms of the frequency spacings for both ways of parameterization. However, as shown below, the partially linear profile was found to erroneously represent the static properties of the measured profile, so the "linear and lumped" profile is of primary interest. Figure 12 depicts the sensitivity of the "linear and lumped" profile. The point of origin for the analysis was the initial set of parameters for this profile given in Table 1 and all three parameters were varied between 90 to 120% of their initial value. The starting thickness h_0 of the profile has proportionally higher influence on the frequency spacings than the other two parameters and is therefore varied to a lesser extent. The graph shows that it is not possible to match the frequency spacing of the measured profile in all four modes exactly, but it is very well possible to lower the deviation considerably. The second set of parameters for the "linear and lumped" profile given in Table 1 were found by using this sensitivity information to achieve better agreement.

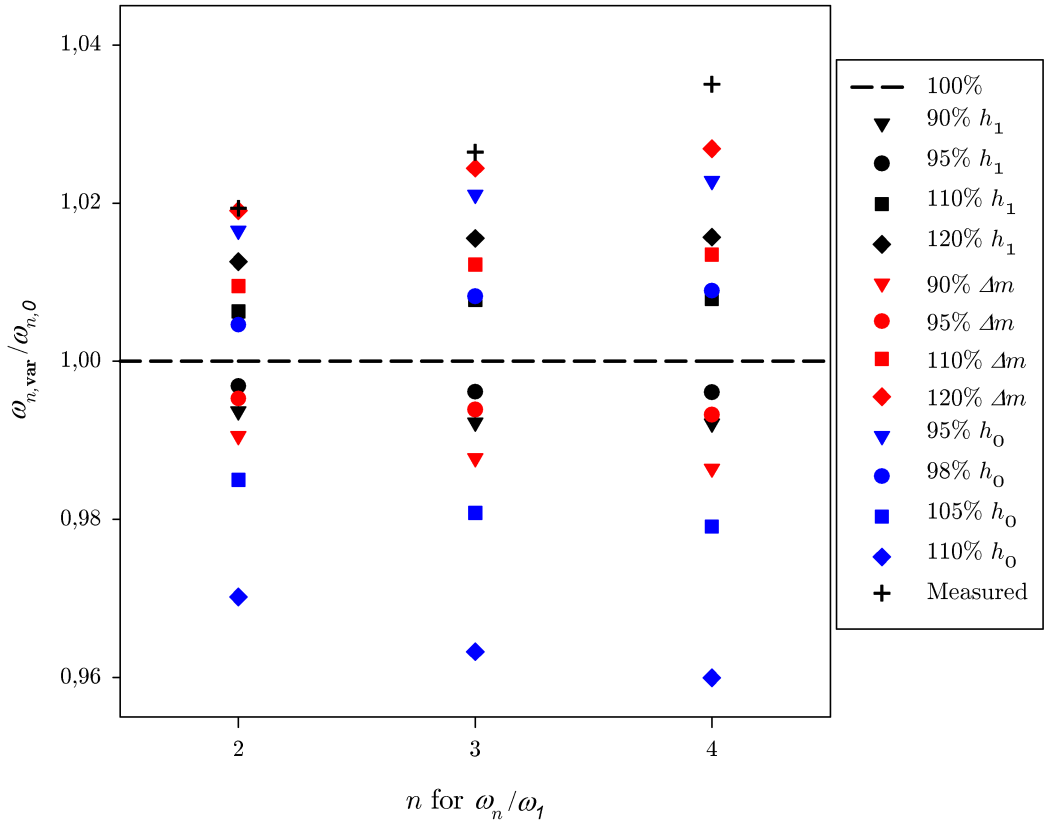

Figure 12.: Variations in h_0, h_1 and Δm parameters of the "Linear and Lumped" profile showing the sensitivity of the frequency spacing with respect to these parameters.

4. Modified Calibration Methods

4.1. Modification of the Sader Method

The Sader method can be modified to include the effect of a massive tip and a non-uniform thickness with the help of the Ritz method [2]. To this end, we introduce an equivalent thicknesses with respect to stiffness and inertia, $h^3_{\mathrm{ek},n}$ and $h_{\mathrm{em},n}$ which are defined as the following

$$h^3_{\mathrm{ek},n} = \frac{\int_0^1 h(x)^3 \left(\psi_n''\right)^2 \mathrm{d}x}{\int_0^1 \left(\psi_n''\right)^2 \mathrm{d}x} \qquad h_{\mathrm{em},n} = \frac{\int_0^1 h(x) \left(\psi_n\right)^2 \mathrm{d}x}{\int_0^1 \left(\psi_n\right)^2 \mathrm{d}x}\,. \tag{14}$$

The equivalent thicknesses, h_{em} and h_{ek}, are the thicknesses of a uniform cantilever would have to produce the same stiffness and inertia coefficients in a single-term Ritz model as the non-uniform beam. These coefficients are introduced into the calibration method.The reader is referred to the appendix (section A.5) for a step-by-step derivation of the modified expression for the spring constant. Following the algebra given in this derivation, one obtains a modified equation for the static stiffness of the probe.

$$k_{\mathrm{s,Sader}} = \frac{3\pi}{4}\rho_{\mathrm{f}}\, b^2 L \Gamma_{\mathrm{i}} \left(\frac{h_{\mathrm{es}}}{h_{\mathrm{ek},n}}\right)^3 \frac{m_{nn}}{k_{nn}}\, Q\, \omega_n^2 \tag{15}$$

This expression is also valid for a uniform probe with a rigid tip, as presented in [2], and for a uniform probe without a tip it reduces to the formula given by Sader. If the thickness profile of a probe is known, then one can compute h_{es}, and with the mode shapes one can compute m_{nn}, k_{nn}, and $h_{\mathrm{ek},n}$. Then, this expression would give an accurate estimate of the spring constant, even in the presence of non-uniformity. Unfortunately, these quantities are not known in practice, so it is difficult to determine the needed constants. One must, instead, make a simplifying assumption regarding the cantilever, such as uniform thickness, in order to obtain an estimate for k_{s}. Our primary purpose for deriving eq. (15) is to estimate the error incurred by such an assumption. Consider an exact solution for the thickness profile and mode shapes. Denote the parameters for that model as h_{es}, $h_{\mathrm{ek},n}$, m_{nn}, and k_{nn}. These parameters would produce the true static stiffness if used in conjunction with the measured Q and

δk_s	Mode 1	Mode 2	Mode 3	Mode 4
Uniform No Tip - Measured	-2.22%	2.62%	6.24%	14.23%
Uniform + Tip - Measured	-2.71%	4.14%	15.91%	25.38%
Linear and Lumped - Measured	-0.06%	5.91%	10.52%	15.43%
Linear and Lumped #2 - Measured	-0.22%	6.00%	9.66%	14.09%

Table 5.: Error in the static stiffness estimated by the method of Sader for various profiles as a function of the mode number used in the calibration. The model based on the measured profile was taken to be exact.

ω_n. An approximate model gives different values for these parameters, which shall be distinguished with hats ($\hat{}$). Then, the error incurred in the Sader method due to the simplifying assumption is given by the following.

$$\delta k_{s,\mathrm{Sader}} = \frac{\hat{k}_s^{\mathrm{model}} - k_s^{\mathrm{true}}}{k_s^{\mathrm{true}}} = \left(\frac{\hat{h}_{es}}{h_{es}}\frac{h_{ek,n}}{\hat{h}_{ek,n}}\right)^3 \frac{\hat{m}_{nn}}{m_{nn}}\frac{k_{nn}}{\hat{k}_{nn}} - 1 \tag{16}$$

The Ritz mode shapes found previously for the measured profile were found to correspond well with the experimentally measured mode shapes shown in [1], so that model will be assumed to be exact and used to compute the error in approximating the probe with each of the models listed in table 1. The resulting relative errors for each of the models are given in table 5 and visualized in figure 13. One observes that each of the models is capable of estimating the static stiffness of the probe to within 3% if the first mode is used in the calibration, and to within 6% if the second is used, although the errors become significantly larger if modes 3 or 4 are used. These modes are more sensitive because the tip mass and the stiffened section of the probe near the tip begins to have an important effect on the mode shapes. It is also interesting to note that the original Sader model of a uniform beam without tip has smaller deviations from the measured profile than the model with a tip. Considering that the tip adds inertia to the model, Sader's original uniform cantilever is less stiff and lacks the inertial effect of the tip at the same time, leading to a mutual compensation in the calibration process and less deviation.

4.2. Modification of the Thermal Tune Method

The Thermal Tune method is based on equivalence between the mean-square potential energy of the cantilever and $\frac{1}{2}\, k_B\, T$.

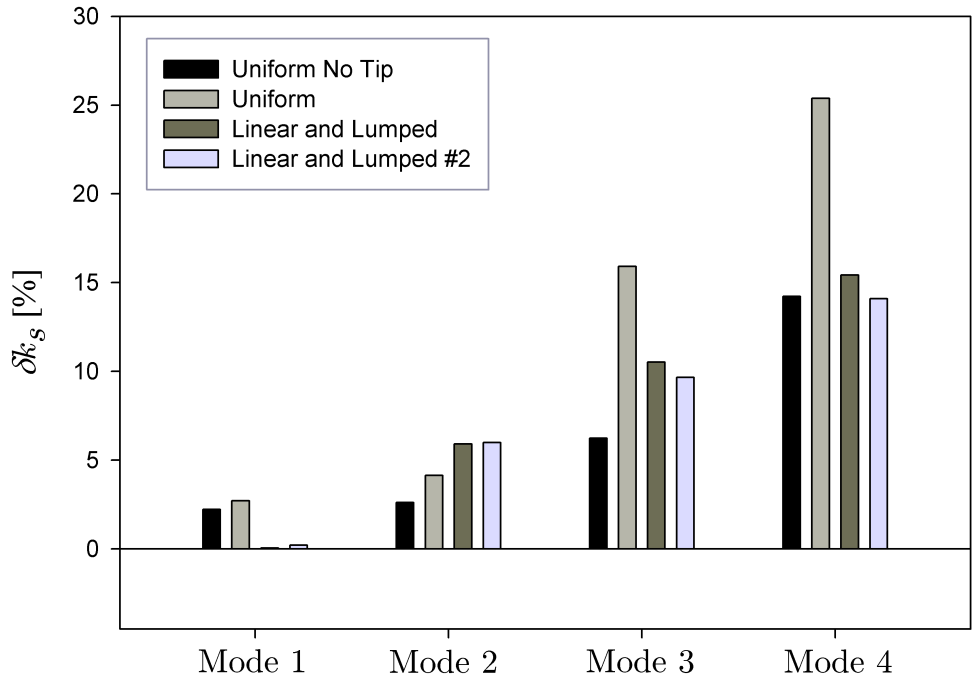

Figure 13.: Visualization of the errors for the Thermal Tune calibration given in table 5.

$$\langle E_{\mathrm{vib}} \rangle = \frac{1}{2} k_{\mathrm{B}} T = \frac{1}{2} \left\langle \int_0^L EI(x) \left(\frac{\partial^2 w}{\partial x^2} \right)^2 \mathrm{d}x \right\rangle \tag{17}$$

The kinetic energy is related to the motion of the tip of the cantilever, which is related to the output signal of the photodiode. However, the sensitivity of the photodiode is measured under static conditions and the shape of a cantilever under static loading is different from its shape when vibrating freely. This is accounted for using the method described by Cook et al. [8], which multiplies the deflection d_{c}^* measured by the photodetector with the factor χ to yield the actual deflection d_{c} needed for the calibration. The slope of the cantilever at x_{l}, where the laser is reflected on the beam, determines the laser spot's position on the photodetector [8]. Hence, χ depends on the ratio of the end-loaded slope W'_{end} to the freely oscillating slope W'_{free},

$$\chi(x_{\mathrm{l}}) = \frac{W'_{\mathrm{end}}(x_{\mathrm{l}})}{W'_{\mathrm{free}}(x_{\mathrm{l}})}. \tag{18}$$

W is the cantilever's normalized shape[1], i.e. the normalized deflection curve in case of the end-loaded cantilever [8] and the normalized mode shape of a freely vibrating cantilever

[1]Normalized shape implies $W(1) \equiv 1$.

is given by $W_{\text{free}}(x) = \psi(x)/\psi(1)$. Following the same approach used to derive the modified Sader method (see section A.6 in the appendix for the Thermal Tune method), the Thermal Tune relationship between the static stiffness and the probe parameters is [1]

$$k_{\text{s,Thermal}} = \frac{3k_{\text{B}}T}{\langle (d_{\text{c}}^*)^2 \rangle} \left(\frac{h_{\text{es}}}{h_{\text{ek,n}}} \right)^3 \left(\frac{\psi_n'(1)^2}{k_{nn} \left(W_{\text{end}}'(1) \right)^2} \right). \tag{19}$$

Likewise, the error induced by non-uniformity in the Thermal Tune method is

$$\delta k_{\text{s,Thermal}} = \frac{\hat{k}_{\text{s}}^{\text{model}} - k_{\text{s}}^{\text{true}}}{k_{\text{s}}^{\text{true}}} = \left(\frac{\hat{h}_{\text{es}}}{h_{\text{es}}} \frac{h_{\text{ek},n}}{\hat{h}_{\text{ek},n}} \right)^3 \left(\frac{W_{\text{end}}'}{\hat{W}_{\text{end}}'} \bigg|_{x=1} \right)^2 \left(\frac{\hat{\psi}_n'(1)}{\psi_n'(1)} \right)^2 \frac{k_{nn}}{\hat{k}_{nn}} - 1, \tag{20}$$

where the hats (ˆ) once again denote the entities for the model of interest. The normalized deflection curve and its derivative for a uniform cantilever are known [8]. The derivative of the deflection curve for a cantilever with an arbitrary thickness profile is calculated using the analytical model for the static deflection of a non-uniform model, which was also used to derive eq. (8).

$$W_{\text{end}}'(x) = \frac{\int_0^x \frac{(x-1)}{h(x)^3} \mathrm{d}x}{\int_0^1 \int_0^{\tilde{x}} \frac{(\tilde{x}-1)}{h(\tilde{x})^3} \mathrm{d}\tilde{x} \mathrm{d}x} \tag{21}$$

The deflection curves and their derivatives with respect to x are given in figure 15 for both the uniform and the measured thickness profiles. It can be observed that the slopes are considerably different near the free end, and this difference is squared in eqs. (19) and (20), so it may be important. The rotation of the mode shapes, $\psi_n'(1)$, i.e. the shape of the freely vibrating cantilever, also induces error in the Thermal Tune method. The slope at the free end of the cantilever is influenced by the profile of the beam, as was illustrated in figure 11.

Table 6 presents the errors in the Thermal Tune estimated spring constant once again using the thickness profile from the SEM images as the "true" model, also depicted in figure 14. In contrast with the Sader method, the thermal method is significantly in error if a uniform probe model is used, even if the first mode is used in the calibration. The error becomes truly unacceptable if the second or higher modes are used. In contrast, the linear and lumped models are acceptably accurate for the first mode but even they become very inaccurate if the third or higher modes are used.

δk_s	Mode 1	Mode 2	Mode 3	Mode 4
Uniform No Tip - Measured	15.31%	72.79%	160.93%	287.70%
Uniform + Tip - Measured	22.53%	71.88%	134.93%	214.03%
Linear and Lumped - Measured	6.32%	13.82%	35.79%	73.20%
Linear and Lumped #2 - Measured	4.64%	8.87%	28.21%	63.07%

Table 6.: Error in the static stiffness estimated by the Thermal Tune method for various profiles as a function of the mode number used in the calibration. The model based on the measured profile was taken to be exact.

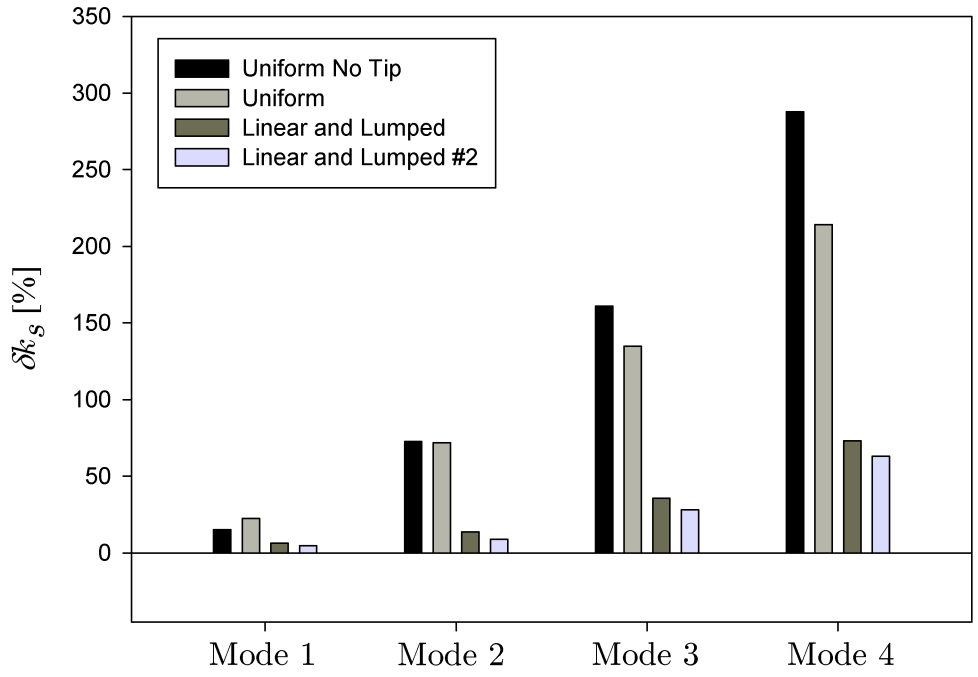

Figure 14.: Visualization of the errors for the Thermal Tune calibration given in table 6.

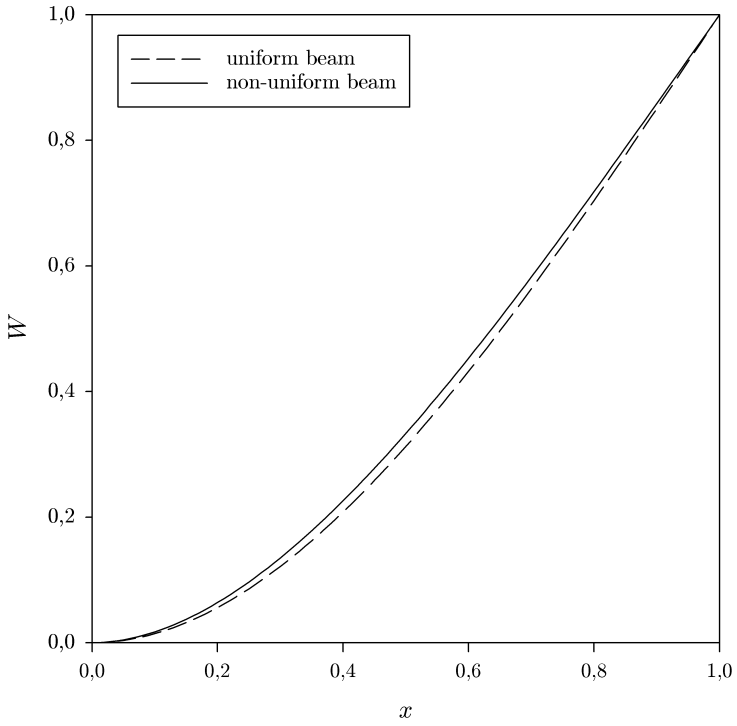

(a)

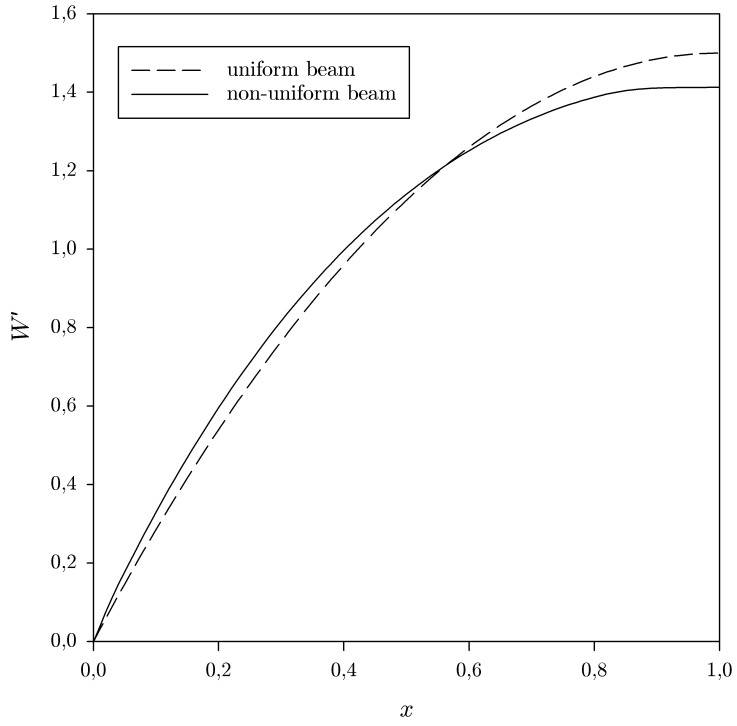

(b)

Figure 15.: Deflection curves of uniform and non-uniform cantilevers under static loading in (a) and the derivative with respect to x, i.e. the slope of the cantilever, in (b).

5. Conclusion and Outlook

The thickness profile of a cantilever has a decisive influence on its static stiffness as well as its mode shapes. Two common AFM calibration methods were analyzed to see how these effects influence the calibration process. The Sader method was found to accurately estimate the static stiffness of the probe under study, but only if the first mode was used in the calibration. One can presume that similar trends would hold for other probes so long as the non-uniformity is not too drastic, thus the Sader method seems to be quite a robust choice. The Thermal Tune method, on the other hand, depends on the rotation of the cantilever under static and dynamic loading and so it was found to be very sensitive to the probe's non-uniformity. These results suggest that the thermal method should not be trusted unless the probe of interest is known to be uniform. A few simple models were explored in an effort to capture the effect of thickness non-uniformity. The models were found to reproduce the natural frequencies and mode shapes of the probe reasonably well, but calibration is sensitive to the model. The "linear and lumped" model did reduce the error in the Thermal Tune calibration to a certain extent, but even then the results showed that one may only be able to trust the calibration based on either the first or perhaps the second mode of the probe. This study presents an approach to analyze calibration errors due to non-uniformity regarding static and dynamics properties. Future works should seek to characterize other probes as was done here for the CSC38 probe, to see whether any of the models proposed here can account for the range of commonly encountered non-uniformities with sufficient fidelity.

Bibliography

[1] M. S. Allen, H. Sumali, P. Penegor. Effect of Tip Mass on Atomic Force Microscope Calibration by Thermal Method. In: *27th International Modal Analysis Conference, Orlando, Florida* (2009) .

[2] M. S. Allen, H. Sumali, P. C. Penegor. Experimental/Analytical Evaluation of the Effect of Tip Mass on Atomic Force Microscope Calibration. *Journal of Dynamic Systems, Measurement, and Control* **131** (2009) 064501. doi: 10.1115/1.4000160.

[3] G. Binnig, C. F. Quate, C. Gerber. Atomic Force Microscope. *Physical Review Letters* **56** (1986) 930–933.

[4] G. Binnig, H. Rohrer, C. Gerber, E. Weibel. Surface Studies by Scanning Tunneling Microscopy. *Physical Review Letters* **49** (1982) 57–61.

[5] N. A. Burnham, X. Chen, C. S. Hodges, G. A. Matei, E. J. Thoreson, C. J. Roberts, M. C. Davies, S. J. B. Tendler. Comparison of Calibration Methods for Atomic Force Microscopy Cantilevers. *Nanotechnology* **14** (2003) 1–6.

[6] H. J. Butt, M. Jaschke. Calculation of Thermal Noise in Atomic Force Microscopy. *Nanotechnology* **6** (1995) 1–7.

[7] J. P. Cleveland, S. Manne, D. Bocek, P. K. Hansma. Nondestructive method for determining the spring constant of cantilevers for scanning force microscopy. *Review of Scientific Instruments* **64** (1993) 403–405.

[8] S. M. Cook, T. E. Schaeffer, K. M. Chynoweth, M. Wigton, R. W. Simmonds, K. M. Lang. Practical Implementation of Dynamic Methods for Measuring Atomic Force microscpoe Cantilever Spring Constants. *Nanotechnology* **17** (2006) 2135–2145. doi:10.1088/0957-4484/17/9/010.

[9] S. Cross, Y. S. Jin, J. R. andf J. K. Gimzewski. Nanomechanical analysis of cells from cancer patients. *Nature Nanotechnology* **2** (2007) 780–783.

[10] Y. F. Dufrene. Towards Nanomicrobiology using Atomic Force Microscopy. *Nature Review Microbiology* **6** (2008) 674–680. doi:10.1038/nrmicro1948.

[11] H. Frentrup, M. S. Allen. Error quantification in calibration of AFM probes due to non-uniform cantilevers. In: *28th International Modal Analysis Conference, Orlando, Florida* (2010) .

[12] M. K. Ghatkesara, E. Rakhmatullinab, H. P. Langa, C. Gerbera, M. Hegnera, T. Brauna. Multi-parameter Microcantilever Sensor for Comprehensive Characterization of Newtonian Fluids. *Sensors and Actuators B: Chemical* **135** (2008) 133–138.

[13] J. H. Ginsberg. *Advanced Engineering Dynamics*. Cambridge University Press, Cambridge, UK (1998).

[14] J. H. Ginsberg. *Mechanical and Structural Vibrations: Theory and Applications*. John Wiley & Sons, New York, USA (2001).

[15] L. Gross, F. Mohn, N. Moll, P. Liljeroth, G. Meyer. The Chemical Structure of a Molecule Resolved by Atomic Force Microscopy. *Science* **325** (2009) 1110–1114.

[16] J. L. Hutter, J. Bechhoefer. Calibration of Atomic Force Microscope Tips. *Review of Scientific Instruments* **64** (1993) 1868–1873.

[17] I. Larson, J. Ralston. *Encyclopedia of Surface and Colloid Science: Colloid Interaction Forces and Atomic Force Microscopy*. CRC Press (2006).

[18] J. E. Sader. Frequency Response of Cantilever Beams immersed in Viscous Fluids with Applications to the Atomic Force Microscope. *Journal of Applied Physics* **84** (1998) 64–76.

[19] J. E. Sader, J. W. M. Chon, P. Mulvaney. Calibration of Rectangular Atomic Force Microscope Cantilevers. *Review of Scientific Instruments* **70** (1999) 3967–3969. doi:10.1063/1.1150021.

[20] J. E. Sader, I. Larson, P. Mulvaney, L. White. Method for the Calibration of Atomic Force Microscope Cantilevers. *Review of Scientific Instruments* **66** (1995) 3789–3798.

[21] J. E. Sader, L. White. Theoretical Analysis of the Static Deflection of Plates for Atomic Force Microscope Applications. *Journal of Applied Physics* **74** (1993) 1–5.

[22] N. D. Spencer, S. P. Jarvis. *Encyclopedia of Chemical Physics and Physical Chemistry: Scanning Probe Microscopies*. Institute of Physics Publishing, London (2001).

[23] Y. Sugimoto, P. Pou, O. Custance, P. Jelinek, M. Abe, R. Perez, S. Morita. Complex Patterning by Vertical Interchange Atom Manipulation using Atomic Force Microscopy. *Science* **322** (2008) 413–417.

[24] S. P. Timoshenko. *History of Strength of Materials*. McGraw-Hill Book Company, New York (1953).

[25] A. Touhami, M. H. Jericho, T. J. Beveridge. Atomic Force Microscopy of Cell Growth and Division in Staphylococcus aureus. *Journal of Bacteriology* **186** (2004) 3286–3295.

Appendices

A. Appendices

A.1. Parameterized profiles

The linear and lumped profiles can be described by the following equation in terms of the thickness variation of the cantilever. The parameters of this profile are a certain base thickness h_0, the linear taper h_1 and an extra lumped mass Δm.

$$h(x) = h_0 + h_1 x \ , \qquad 0 \leq x \leq 1 \tag{22}$$

The lumped inertial contribution Δm of the considerable taper that cannot be mimicked by a moderate taper is calculated with the help of the measured profile.

$$\Delta m = \rho b L \int_0^1 h_{\text{measured}}(x) - h(x) \mathrm{d}x \tag{23}$$

The partially linear profile is given by equation (24). The parameters of this particular profile are a certain nominal thickness h_{nom}, the thickness $h(1)$ at the end of the beam and the position x_0 where the taper starts.

$$h(x) = \begin{cases} h_{\text{nom}} & 0 \leq x < x_0 \\ h_{\text{nom}} + h_1 \left(x - x_0\right) & x_0 \leq x \leq 1 \end{cases} \qquad \text{with} \quad h_1 = \frac{h(1) - h_{\text{nom}}}{1 - x_0} \tag{24}$$

A.2. Analytical approach for the static stiffness of a non-uniform cantilever

Following classical beam theory, the spring constant[1] of a uniform cantilever is dependent on the beam's dimensions and it's Young's modulus, $k_{\text{s}} = {}^{Ebh^3}/_{4L^3}$. The thickness h of the beam must be uniform along the length for this expression to hold. For the respective expression that also holds for rectangular cantilevers of an arbitrary thickness, one must analyze a statically end-loaded cantilever. The deflection of an Euler-Bernoulli beam

[1] In detail, $k_{\text{s}} = {}^{3EI}/_{L^3}$, where I is the beam's second moment of area $I = {}^{bh^3}/_{12}$.

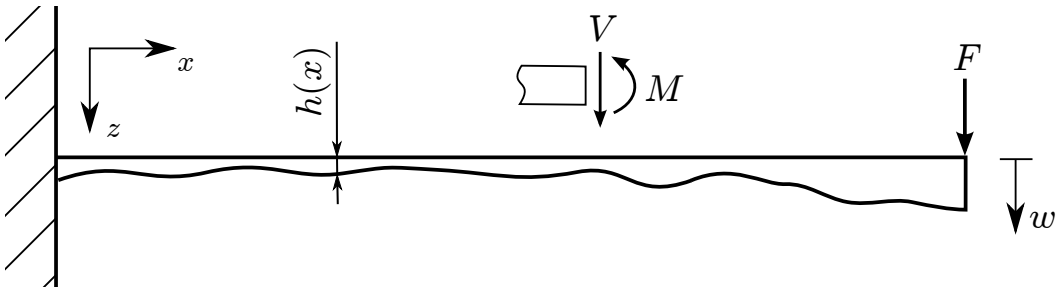

Figure 16.: Cantilever beam of arbitrary thickness and a schematic of the sign convention used in the derivation.

under static loading is governed by the moments acting on the beam [24].

$$w''(x) = -\frac{M(x)}{EI(x)} \qquad \Rightarrow \qquad w(x) = L^2 \int\int \frac{M(x)}{EI(x)} \mathrm{d}x\mathrm{d}x + c_1 x + c_2 \tag{25}$$

For a clamped-free cantilever, deflection and rotation of the beam do not occur at the left boundary, where Dirichlet and von Neumann boundary conditions apply, $w(0) = 0,\ w'(0) = 0$. These boundary conditions yield $c_1 = 0,\ c_2 = 0$. Since the cantilever is under static loading by an arbitrary constant force F acting at the cantilever's end, the bending moment is linear, meaning $M(x) = FL(x-1)$. Thus,

$$w(x) = FL^3 \int\int \frac{(1-x)}{EI(x)} \mathrm{d}x\mathrm{d}x. \tag{26}$$

The definition of the spring constant is force per unit deflection, $k_\mathrm{s} = {}^F\!/_w$. From equation (26), it is apparent that

$$\begin{aligned} k_\mathrm{s} &= \frac{1}{L^3}\left[\int_0^1 \int_0^x \frac{(1-\tilde{x})}{EI(\tilde{x})} \mathrm{d}\tilde{x}\mathrm{d}x\right]^{-1} \\ &= \frac{Eb}{12L^3}\left[\int_0^1 \int_0^x \frac{(1-\tilde{x})}{h(\tilde{x})^3} \mathrm{d}\tilde{x}\mathrm{d}x\right]^{-1}. \end{aligned} \tag{27}$$

Based on this result, the equivalent thickness h_es can be definied. It is the thickness of a uniform cantilever with the same spring constant as the non-uniform cantilever under consideration. The spring constant of a non-uniform cantilever is therefore

$$k_\mathrm{s} = \frac{Ebh_\mathrm{es}^3}{4L^3}, \tag{28}$$

$$h_\mathrm{es}^3 = \frac{1}{3}\left[\int_0^1 \int_0^x \frac{(1-\tilde{x})}{h(\tilde{x})^3} \mathrm{d}\tilde{x}\mathrm{d}x\right]^{-1}. \tag{29}$$

A.3. Solution for the Euler-Bernoulli beam equation with a tip

The flexural motion of an Euler-Bernoulli beam is governed by the following partial differential equation (PDE)

$$\frac{\partial^2}{\partial x^2}\left(EI\frac{\partial^2 w}{\partial x^2}\right) + \rho A\ddot{w} = q_z \ , \tag{30}$$

where E denotes Young's modulus, I the area moment of inertia and ρ and A are the density and the cross-section area of the cantilever, repectively [14]. An approach for a cantilever with a varying thickness is given in section 3.2.2. At this point, these properties are considered to be constant. For a freely vibrating cantilever, the force per unit length loading, q_z, is zero. Moreover, the eigenmodes of the structure are of interest, so we apply no external loads to the beam.

The general Euler-Bernoulli beam theory considers the flexural motion of the beam to be small. This is certainly the case for an AFM probe, where vibration amplitudes are in the order of magnitude of a few nanometers. Shear deformation of the beam as well as the rotary inertia are neglected in the Euler-Bernoulli beam. This results in inaccuracies when considering higher modes. The first four modes of the structure were analyzed in this study, though.

A separation of variables approach is employed to convert the problem into a ordinary differential equation (ODE).

$$w(x,t) = \mathrm{Re}\left\{\psi(x)\, e^{i\omega t}\right\} \tag{31}$$

Thus, the approach yields

$$\frac{\partial^4 \psi_n(x)}{\partial x^4} + \alpha_n^4 \psi_n(x) = 0 \ , \quad \text{with} \quad \alpha_n = \sqrt[4]{\frac{\rho A \omega_n^2 L^4}{EI}} \ . \tag{32}$$

A general solution for $\psi_n(x)$ is given by

$$\psi_n(x) = C_1 \sin(\alpha_n x) + C_3 \sinh(\alpha_n x) + C_2 \cos(\alpha_n x) + C_4 \cosh(\alpha_n x) \tag{33}$$

At this point, we know neither the coefficients C_j nor the modal parameter α_n. The solution still remains to satisfy the boundary conditions. Therefore, the choice of boundary conditions is crucial as they not only determine both the modal parameter α_n and the parameters C_j, but also the properties of the tip attached to the end of the can-

tilever are incorporated into the problem through the boundary conditions. Since the left boundary is a fixed end, there is neither deflection nor rotation at this end. These Dirichlet and von Neumann boundary conditions, which apply for a fixed-free cantilever, allow the elimination of two of the parameters C_j.

$$w(0) = 0, \left.\frac{\partial w}{\partial x}\right|_{x=0} = 0 \quad \Rightarrow \quad \psi(0) = 0, \left.\frac{\partial \psi}{\partial x}\right|_{x=0} = 0 \tag{34}$$

By substituting eq. (33) into these boundary conditions, two parameters can be eliminated since $C_4 = -C_2$ and $C_3 = -C_1$. Therefore, the analytical mode shape of the cantilever is

$$\psi_n(x) = C_1 \left[\sin(\alpha_n x) - \sinh(\alpha_n x)\right] + C_2 \left[\cos(\alpha_n x) - \cosh(\alpha_n x)\right]. \tag{35}$$

For a regular clamped-free cantilever, the right boundary with no acting moments and forces could simplify the problem further. In this particular case though, the inertial effects of the tip attached to the end of the cantilever must be taken into account in the boundary conditions as they alter the mode shapes and natural frequency of the vibrating beam. To this end, a balance of shear forces and moments at the right boundary gives a set of mixed boundary conditions.

A consistent sign convention is very important and the convention applied here is the same as in [14], Ch. 7 (pg. 422). The balance of shear forces S at the tip end considers the inertia of the tip mass m_{tip} and yields the right boundary condition, $-S = m_{\text{tip}}\ddot{w}(1)$.

$$\left.\frac{\partial}{\partial x}\left(\frac{EI}{L^3}\frac{\partial^2 w(x)}{\partial x^2}\right)\right|_{x=1} = -m_{\text{tip}}\omega^2 w(1)$$

$$\frac{EI}{L^3}\psi'''(1) = -m_{\text{tip}}\omega^2\psi(1) \tag{36}$$

With $m_{\text{beam}} = \rho AL$, one can express the boundary condition as follows

$$\psi'''(1) + \alpha^4 \left(\frac{m_{\text{tip}}}{m_{\text{beam}}}\right)\psi(1) = 0. \tag{37}$$

The rotary effects of the tip taken into account by the moment balance at the end of the beam serves as the remaining boundary condition for the problem, $M = \frac{J_{\text{tip}}}{L}\left.\frac{\partial \ddot{w}(x)}{\partial x}\right|_{x=1}$.

$$\left.\left(\frac{EI}{L^2}\frac{\partial^2 w(x)}{\partial x^2}\right)\right|_{x=1} = \frac{-J_{\text{tip}}\omega^2}{L}\left.\left(\frac{\partial w(x)}{\partial x}\right)\right|_{x=1}$$

$$\frac{EI}{L^2}\psi''(1) = -\frac{J_{\text{tip}}\omega^2}{L}\psi'(1) \tag{38}$$

where J_{tip} denotes the tip's moment of inertia. We therefore obtain

$$\psi''(1) + \alpha^4 \left(\frac{J_{\text{tip}}}{m_{\text{beam}}L^2}\right)\psi'(1) = 0. \tag{39}$$

The set of equations given by (37) and (39) form a complete set of boundary conditions for the PDE (32), which is necessary to obtain the solution of the PDE. These boundary conditions still depend on the modal parameter α. We substitute eq. (35) into the remaining set of boundary conditions.

$$[\mathbf{D}(\alpha)] \cdot (\mathbf{C}) = \mathbf{0} \tag{40}$$

In order for eq. (40) to have a non-trivial solution for $(\mathbf{C})$, it is necessary that $|[\mathbf{D}(\alpha)]| = 0$. The modal parameters α_n are therefore the roots of the characteristic polynomial of $|[\mathbf{D}(\alpha)]| = 0$. Looking back to eq. (32), we can determine the natural frequencies of the cantilever.

$$\omega_n = \sqrt{\frac{EI\alpha_n^4}{\rho A L^4}} \tag{41}$$

A.4. Applying the Ritz method to the AFM cantilever problem

As discussed in the previous section, the cantilever beam being a continuous system can be analyzed with a field equation approach. The approach of the Ritz method is to map a continuous function, such as displacement, into an N-dimensional space of basis functions. What is more, this set of basis functions can separate the spatial and time-dependence of the original function. The generalized coordinates are chosen to be time-dependent only.

$$\mathsf{w}(x,t) = \sum_{j=1}^{N} \psi_j(x)\mathsf{q}_j(t) \quad \Longleftrightarrow \quad w(x,\omega) = \sum_{j=1}^{N} \psi_j(x)q_j(\omega)$$

It shall be noted that the frequency domain expression of time-dependent generalized coordinates is equally valid and more useful than a derivation in the time domain in this

particular case.[1] The resulting formulation of the kinetic energy T and potential energy V of the system reveals that through the Ritz approach, one can treat a continuous system of distributed degrees of freedom as a discrete N-degree-of-freedom system, where N is the number of the basis functions we chose to map the continuous variable.

$$T = \frac{1}{2}\sum_{j=1}^{N}\sum_{n=1}^{N} M_{jn}\dot{q}_j\dot{q}_n \qquad V = \frac{1}{2}\sum_{j=1}^{N}\sum_{n=1}^{N} K_{jn}q_j q_n$$

Here, M_{jn} and K_{jn} denote the inertia and stiffness coefficients, respectively. Having said this, the equations of motion for the cantilever take the common form of

$$[\mathbf{M}](\ddot{\mathbf{q}}) + [\mathbf{C}](\dot{\mathbf{q}}) + [\mathbf{K}](\mathbf{q}) = (\mathbf{Q}). \tag{42}$$

For a freely vibrating cantilever, the excitation on the right-hand-side of equation (42) can be neglected.

It is essential to determine the inertia, damping and stiffness matrix of the system. Starting with the inertia coefficients, one must consider everything that contributes to the kinetic energy of the system.

$$M_{jn} = \int_0^1 \rho A L\, \psi_j\psi_n \mathrm{d}x + \sum m\, \psi_j(x_\mathrm{m})\psi_n(x_\mathrm{m}) + \sum \frac{I_\mathrm{m}}{L^2}\left(\frac{\partial\psi_j}{\partial x}\,\frac{\partial\psi_n}{\partial x}\right)\Bigg|_{x=x_\mathrm{m}} \tag{43}$$

The first contribution to the inertia coefficients is the cantilever's inertia. For the specific case of a microprobe cantilever, the mass and rotary inertia of the tip are attached at the end of the cantilever and accounted for in the non-integral terms.

$$M_{jn,\mathrm{beam}} = \rho b L \int_0^1 h(x)\,\psi_j\psi_n \mathrm{d}x + m_\mathrm{tip}\,\psi_j(1)\psi_n(1) + \frac{I_\mathrm{tip}}{L^2}\left(\frac{\partial\psi_j}{\partial x}\,\frac{\partial\psi_n}{\partial x}\right)\Bigg|_{x=1} \tag{44}$$

As mentioned in section 2.1, the effects of the fluid add a virtual mass to the cantilever, which is describes by the real part of the hydrodynamic force. The inertial effects of the fluid are then given by

$$M_{jn,\mathrm{fluid}} = \frac{\pi}{4}\rho_\mathrm{f}\, b^2 L \Gamma_\mathrm{r}(\omega) \int_0^1 \psi_j\psi_n \mathrm{d}x. \tag{45}$$

The resulting inertial coefficients are the sum of the different contributions, $M_{jn} = M_{jn,\mathrm{beam}} + M_{jn,\mathrm{fluid}}$. If material damping is neglected, the only form of dissipation stems from the fluid damping which can be expressed with the hydrodynamic force, and thus

[1] The Fourier transform can be used to bring time domain quantities into the frequency domain, $X(\omega) = \int_{-\infty}^{\infty} X e^{i\omega t} dt$.

$$C_{jn} = C_{jn,\text{fluid}} = \frac{\pi}{4}\rho_\text{f}\, b^2 L \Gamma_\text{i}(\omega) \int_0^1 \psi_j \psi_n \mathrm{d}x. \tag{46}$$

Finally, the assessment of the stiffness of the beam is very comprehensive as no additional springs are attached to the cantilever. The stiffness coefficients of the cantilever are

$$K_{jn} = \frac{Eb}{12L^3} \int_0^1 h(x)^3 \frac{\partial^2 \psi_j}{\partial x^2} \frac{\partial^2 \psi_n}{\partial x^2} \mathrm{d}x. \tag{47}$$

To abbreviate these expressions, we define the following coefficients

$$m_{jn} = \int_0^1 \psi_j \psi_n \mathrm{d}x \qquad k_{jn} = \int_0^1 \frac{\partial^2 \psi_j}{\partial x^2} \frac{\partial^2 \psi_n}{\partial x^2} \mathrm{d}x \tag{48}$$

$$h_{\text{em},jn} = \frac{1}{m_{jn}} \int_0^1 h(x) \psi_j \psi_n \mathrm{d}x \qquad h^3_{\text{ek},jn} = \frac{1}{k_{jn}} \int_0^1 h(x)^3 \frac{\partial^2 \psi_j}{\partial x^2} \frac{\partial^2 \psi_n}{\partial x^2} \mathrm{d}x \tag{49}$$

Therefore, the complete set of inertial, damping and stiffness coefficients in the EOM of the Ritz method is

$$M_{jn} = \rho b L (h_{\text{em},jn} m_{jn}) + \left[\frac{\pi}{4}\rho_\text{f} b^2 L \Gamma_\text{r}(\omega)\right] m_{jn} + m_\text{tip} \psi_n(1)^2 + \frac{I_\text{tip}}{L^2} \left(\psi_n'(1)\right)^2 \tag{50}$$

$$C_{jn} = \left[\frac{\pi}{4}\rho_\text{f} \omega b^2 L \Gamma_\text{i}(\omega)\right] m_{jn} \tag{51}$$

$$K_{jn} = \frac{Eb}{12L^3} (h^3_{\text{ek},jn} k_{jn}) \tag{52}$$

Acquiring the eigenmodes and eigenfrequencies entails a solution of the generalized eigenvalue problem.

$$\left[[\mathbf{K}] - \omega^2 [\mathbf{M}]\right] (\phi) = 0 \tag{53}$$

A Ritz series with N terms has N natural frequencies ω_n and N orthogonal modes (ϕ_n). By scaling the computed modes to have a unit modal mass, the mode shapes of the vibrating cantilever are the normalized mode functions

$$(\mathbf{\Phi}_j) = \frac{(\phi_j)}{\left[(\phi_j)^\text{T} [\mathbf{M}] (\phi_j)\right]^{1/2}}. \tag{54}$$

This leads to the first orthogonality property

$$\left[(\mathbf{\Phi}_j)^{\mathrm{T}}[\mathbf{M}](\mathbf{\Phi}_j)\right] = \delta_{jn} \tag{55}$$

and the second orthogonality property allows the computation of the natural frequencies of the cantilever

$$\left[(\mathbf{\Phi}_j)^{\mathrm{T}}[\mathbf{K}](\mathbf{\Phi}_j)\right] = \omega_n^2\,\delta_{jn}. \tag{56}$$

A.5. Derivation of the modified Sader method

The mode shapes and natural frequencies calculated with the Ritz method are approximate solutions for a continuous structure which cannot be approached with analytical methods. However, if the basis functions of the Ritz series were an exact solution to the problem, a single term Ritz series would be an exact model for the contribution of a single mode to a structure's response. Thus, we take a single term Ritz series $N = 1$, for which we employ the nth mode of our beam, to derive the method of Sader. The equation of motion of our problem then boils down to

$$M_{nn}\ddot{q}_n + C_{nn}\dot{q}_n + K_{nn}q_n = 0, \tag{57}$$

with the coefficients given as follows

$$M_{nn} = \rho bL(h_{\mathrm{em},n}m_{nn}) + \left[\frac{\pi}{4}\rho_{\mathrm{f}}b^2L\Gamma_{\mathrm{r}}(\omega)\right]m_{nn} + m_{\mathrm{tip}}\psi_n(1)^2 + \frac{I_{\mathrm{tip}}}{L^2}\left(\psi_n'(1)\right)^2 \tag{58}$$

$$C_{nn} = \left[\frac{\pi}{4}\rho_{\mathrm{f}}\omega b^2L\Gamma_{\mathrm{i}}(\omega)\right]m_{nn} \tag{59}$$

$$K_{nn} = \frac{Eb}{12L^3}(h_{\mathrm{ek},n}^3k_{nn}). \tag{60}$$

The expression for the static stiffness of a non-uniform cantilever[1] from the derivation in section A.2 can be used at this point and equation (60) can be written as

$$K_{nn} = \frac{k_s}{3}\left(\frac{h_{\mathrm{ek},n}}{h_{\mathrm{es}}}\right)^3 k_{nn}. \tag{61}$$

Subsequently, we divide the equation of motion of the single term Ritz approach by M_{nn}. The terms multiplying $\dot{q}_n$ and q_n are ω_n/Q and ω_n^2, respectively. Thus, we obtain

[1] Spring constant of the non-uniform cantilever, $k_s = \frac{Eb{h_{es}}^3}{4L^3}$

$$\frac{k_s}{3}\left(\frac{h_{\mathrm{ek},n}}{h_{\mathrm{es}}}\right)^3 k_{nn} = \omega_0 Q\left[\frac{\pi}{4}\rho_{\mathrm{f}}\omega b^2 L\Gamma_{\mathrm{i}}\right] m_{nn}. \tag{62}$$

It shall be noted that for an under-damped system with $Q >> 1$, which is the case for a cantilever vibrating in air, one can approximate the natural frequency of the damped cantilever to being equal to the undamped case. Therefore, rearranging equation (62) yields an expression for the static stiffness as a function of the natural frequency and the quality factor of the cantilever.

$$k_{\mathrm{s,Sader}} = \frac{3\pi}{4}\rho_{\mathrm{f}} b^2 L\Gamma_{\mathrm{i}}\left(\frac{h_{\mathrm{es}}}{h_{\mathrm{ek},n}}\right)^3 \frac{m_{nn}}{k_{nn}} Q\omega_n^2 \tag{63}$$

A.6. Derivation of the modified Thermal Tune Method

For a freely vibrating microcantilever, mean-square thermal noise oscillations are related to the amplitude of vibration and the spring constant,

$$\frac{1}{2}k_B T = \frac{1}{2}\left\langle \int_0^1 \frac{EI(x)}{L^3}\left(\frac{\partial^2 w}{\partial x^2}\right)^2 \mathrm{d}x \right\rangle \tag{64}$$

The right-hand-side of equation (64) is the potential energy stored in the deformation of a cantilever beam, where w denotes the transverse deflection of the cantilever. Similar to the approach for the Sader method above, a single term basis functions is used to depict the cantilever's vibratory deformation, $w(x,t) = \psi_n(x)q(t)$.

$$k_B T = \frac{Eb}{12L^3}\int_0^1 h(x)^3\left(\frac{\partial^2 \psi_n}{\partial x^2}\right)^2 \mathrm{d}x\ \langle q(t)^2\rangle \tag{65}$$

Using the expression for $h_{\mathrm{ek},n}$ in equation (49) and the spring constant of a non-uniform cantilever in equation (28),

$$
\begin{aligned}
k_B T &= \frac{E b h_{\mathrm{ek},n}^3}{12 L^3}\, k_{nn}\, \langle q(t)^2 \rangle \\
&= \frac{k_s}{3} \left(\frac{h_{\mathrm{ek},n}}{h_{\mathrm{es}}} \right)^3 k_{nn} \langle q(t)^2 \rangle \\
&= \frac{k_s}{3} \left(\frac{h_{\mathrm{ek},n}}{h_{\mathrm{es}}} \right)^3 k_{nn} \frac{\langle \psi(1)^2 q(t)^2 \rangle}{\psi(1)^2} \\
&= \frac{k_s}{3} \left(\frac{h_{\mathrm{ek},n}}{h_{\mathrm{es}}} \right)^3 k_{nn} \frac{\langle d_c^2 \rangle}{\psi(1)^2} \\
&= \frac{k_s}{3} \left(\frac{h_{\mathrm{ek},n}}{h_{\mathrm{es}}} \right)^3 k_{nn} \chi_n^2 \frac{\langle (d_c^*)^2 \rangle}{\psi(1)^2}.
\end{aligned}
$$

In the derivation above, the factor χ is used to account for the difference between the deflection shape of a freely vibrating cantilever to a statically loaded cantilever. A thorough discussion of this can be found in [8]. Following the derivation above, one obtains an expression for the static stiffness of a non-uniform cantilever that contains the mean-square vibratory deflections of the cantilever's end and the temperature at which the cantilever vibrates.

$$
k_{\mathrm{s,Thermal}} = \frac{3 k_{\mathrm{B}} T}{\langle (d_{\mathrm{c}}^*)^2 \rangle} \left(\frac{h_{\mathrm{es}}}{h_{\mathrm{ek,n}}} \right)^3 \left(\frac{\psi_n'(1)^2}{k_{nn} \left(W_{\mathrm{end}}'(1) \right)^2} \right) \tag{66}
$$